Lithospheric Stratigraphy beneath the Southern Rocky Mountains, USA

Brian Zurek and Ken Dueker

Department of Geology and Geophysics, University of Wyoming, Laramie, Wyoming

The Continental Dynamics - Rocky Mountains (CD-ROM) experiment seeks to constrain the evolution, stabilization and modification of the continental lithosphere of the southern Rocky Mountains. In this paper, we present the detailed results of images constructed using broadband teleseismic receiver functions of the continental lithosphere in the interior western United States, with focus on the southern Rocky Mountains. The targets of this experiment are the Cheyenne suture, an Archean continent/Proterozoic arc terrane boundary, and the Jemez suture/volcanic lineament, that separates the Proterozoic Mazatzal and Yavapai provinces. The main features observed across the Cheyenne belt are a thick lithosphere (>150 km) as evidenced by changes in the mantle lithospheric layering across the Cheyenne Suture. Underlying the Cheyenne suture is a Proterozoic oceanic slab fragment, most plausibly tectonically emplaced beneath the rifted Wyoming margin. Below the Jemez volcanic lineament two strong sub-crustal layers are imaged down to 100 km depth that reside within the tomographically imaged low velocity zone. This layering is interpreted to map the depth extent of the lithosphere and most plausibly results from changes in chemical composition of the lithosphere. In contrast to the Cheyenne suture, little evidence is seen beneath the Jemez lineament for a suture that extends through the lithosphere. Our conclusions are that beneath the Archean-Proterozoic Cheyenne belt the lithosphere is at least 150 km thick and preserves 1.7 Ga. lithospheric scale structure, while across the Proterozoic-Proterozoic Jemez boundary, the lithosphere is at least 100 km thick.

1. INTRODUCTION

The study of the continental mantle lithosphere provides insight into the role the sub-crustal lithosphere plays in the creation, stabilization and modification of continents [*O'Reilly et al.*, 2001]. Recent seismic images near suture zones have shown reflectors in the mantle lithosphere most plausibly explained as "fossilized" subducted slabs [*Balling*, 2000; *Bostock*, 1997; *Warner et al.*, 1996]. Tomography of the upper mantle often shows distinct velocity heterogeneity between differing crustal provinces in the upper 100 - 200 km [*Bank et al.*, 2000; *Rondenay et al.*, 2000]. Mantle xenoliths from different age provinces often show significant compositional variations with respect to age [*O'Reilly et al.*, 2001]. These observations suggest that the processes that create, stabilize and modify continental lithosphere involve a poorly constrained mixture of varying bulk compositions and slab fragments.

The Continental Dynamics - Rocky Mountains (CD-ROM) experiment is the study of the geodynamic processes that created the southwestern United States. The creation of this lithosphere resulted from the accretion of Proterozoic island arc terranes to the rifted 2.1 Ga southern margin of the Archean Wyoming craton [*Karlstrom and Houston*, 1984]. The CD-ROM passive seismic experiment targeted two boundaries created by island arc accretion (Plate 1): 1) The Archean-Proterozoic boundary known as the Cheyenne belt, which separates the 2.4-3.9 Ga Wyoming craton from the 1.78-1.74 Ga Yavapai Proterozoic province [*Frost et al.*, 1993]; 2) the Jemez suture, a Proterozoic-Proterozoic boundary, which separates the 1.73 Ga Yavapai province from the 1.65 Ga Mazatzal province [*Karlstrom and Bowring*, 1988].

Today, this ancient lithosphere is being thermally and chemically reworked, as evidenced by xenolith P-T-t studies [*Smith*, 2000], high heat flow [*Morgan and Gosnold*, 1989], late-Cenozoic volcanism [*Thompson et al.*, 1997] and post-Miocene uplift of the southern Rocky Mountains and High Plains [*Thompson and Zoback*, 1979; *Heller* et al., 2003]. Interestingly, this region of lithospheric reworking correlates well with low upper mantle velocities [*Deep Probe working group*, 1998; *Goes and van der Lee*, 2002]. Conversion of these low velocities to thermal structure sug-

gests that most of this regions sub-crustal mantle is at or near the dry peridotite solidus [*Goes and van der Lee*, 2002]. This suggests a casual link between the low velocities and the high heat flow, volcanism and possible late Cenozoic uplift in this region.

Constraining the thickness of the lithosphere is fundamental to understanding the origin of this low velocity region. One popular model suggests that this region is high standing and warm because the lithosphere has been thinned either by: the Laramide slab advecting much of the sub-crustal lithosphere eastward beneath the High Plains [*Bird*, 1988] or delamination of the sub-crustal lithosphere [*Bird*, 1979]. However, this thin lithosphere model does not predict post-Miocene uplift and is inconsistent with thick lithosphere observations: xenolith P-T-t studies [*Smith*, 2000], late-Cenozoic high-K lamprolitic lavas [*Thompson et al.*, 1997] and diamonds from the Stateline Devonian kimberlite pipes [*McCallum et al.*, 1975]. Thus, we propose a thick lithosphere model in which the modern day lithosphere is chemically thick, perhaps hydrated along its sutures, and is presently low velocity because the lithosphere is being reheated by mantle processes [*Dueker et al.*, 2001]. To test this model, new detailed images of mantle layering are presented and synthesized with new tomographic velocity results [*Yuan and Dueker*, this volume].

2. METHOD

Receiver functions are used to isolate receiver side P to S conversions (denoted as a P_ds phase where d is depth to the interface generating the S-wave) created by significant velocity contrasts (Fig. 1). A P_ds conversion is generated when a teleseismic P-wave partitions a small fraction of its amplitude (i.e., <10%) to a S-wave at a relatively sharp velocity gradient. The Moho is usually the largest lithospheric velocity contrast with a 20% change in P-velocity. Receiver functions have been primarily been used to measure crustal thickness by identifying the Moho P_ds arrival. The use of receiver functions to study sub-crustal layering is hindered by: 1) inadequate spatial sampling with broad-band seismometers; 2) signal generated noise: especially, the interference of free surface multiples [*Bostock*, 1996], complex P-S resonance in sedimentary basins [*Levander and Hill*, 1985] and free surface P to Rg topographic scattering [*Clauser and Langston*, 1995]. However, we believe by taking the necessary steps, receiver functions can be used to identify structure in the mantle lithosphere. The problems associated with sub-crustal imaging are mitigated by: 1) deploying arrays with dense 10 km station spacing; 2) stacking the data across many stations via common conversion points stacking of receiver functions (converted-wave equivalent of common mid-point stacks in reflection seismology); 3) the suppression of reverberations by the application of phasing analysis.

2.1 Data set

The CD-ROM natural source seismic experiment consisted of the deployment of 47 PASSCAL broad-band sensors along two transects: CD-ROM North and CD-ROM South (Plate 1). These lines operated for a full year, from June 1999 to June 2000. The data comes from direct P waves with source magnitudes >5.5 and a distance of 20-95° (Fig. 2). The initial set of 2100 waveforms is culled by: 1) requiring the zero-lag P arrival to be the largest arrival on the receiver function, and 2) using receiver functions with RMS values < 20% of the P-arrival. This culling produces a final data set of ~1400 receiver functions.

2.2 Deconvolution

Receiver functions are made via deconvolution of the vertical component from the radial component of the seismogram using water-level spectral division [*Langston*, 1977] with a water-level of 0.1 [*Clayton and Wiggins*, 1976]. The data is windowed from 10 s before to 120 s after the P arrival. To maximize the signal to noise ratio, a zero-phase Butterworth filter with a band-pass of 1.5 - 0.3 Hz is used to isolate P_ds arrivals.

2.3 Mapping Time to Depth

To make a depth image of discontinuity structure in the lithosphere, the time of a P_ds arrival must be mapped to depth. For a flat Earth, this time is simply a function of ray parameter and depth to interface (Fig. 1)[*Gurrola et al.*, 1994]:

$$T_{P_dS}(p,D) = \int_{-D}^{0} \left[\sqrt{V_S(z)^{-2} - p^2} - \sqrt{V_P(z)^{-2} - p^2} \right] dz \quad (1)$$

where D is the depth to interface, V_S is the S-velocity, V_P is the P-velocity and p is the Cartesian ray parameter (s/km). The tectonic 1-D North American shear wave model (TNA) [*Grand and Helmberger*, 1984] is used for $V_S(z)$. $V_P(z)$ is calculated assuming the IASP upper mantle average V_P/V_S of 1.84 [*Kennett and Engdahl*, 1991]. Ray parameter is calculated using the source to receiver distance and the IASPI velocity model. An Earth flattening transformation is applied to correct for the Earth's sphericity.

Note that the relative depth variations are better constrained than the absolute depths. The absolute depths are contingent upon the P- and S- velocity model used for mapping time to depth. False relative depth variation would arise from large, lateral bulk-crustal velocity variations. However, no large-scale P-wave velocity variations are observed in the CD-ROM refraction model [*Snelson and Keller*, this volume]. Furthermore, it is encouraging that the crustal velocity model based on the P-wave refraction model and assuming a Vp/Vs of 1.8 maps the P_dS Moho to within the errors of the refraction model. Therefore, we believe that 1-D velocity model used is an acceptable approximation for mapping time to depth.

2.4 Forward Formulation of the Model Space

To identify velocity discontinuities in the lithosphere, a 2-D model is constructed using the common conversion point (CCP) method [*Dueker and Sheehan*, 1997]. The CCP image is constructed by solving the linear matrix equation:

$$\mathbf{Am} = \mathbf{d}, \quad (2)$$

where **A** is the scattering matrix, **m** is the model vector and **d** is the data vector. The model vector is a 2-D grid of scattering points with 2 by 1 km spacing. The data vector is the concatenation of the radial receiver functions. The scattering matrix is a matrix of zeros and ones that specify which grid points are sampled by the receiver functions. The construction of the scattering matrix is accomplished via 1-D ray tracing downward through the velocity model. To properly account for variations in model sampling, each column of the scattering matrix is normalized by its' column sum. Given that the slowness of a typical P_dS ray path is <4% smaller than the P-wave slowness [*Gurrola et al.*, 1994], it is a good approximation to use the IASPI P-wave slowness value for ray tracing. Note that this formulation ignores diffractions and ray bending. These effects are not considered important to the image quality because 3-D Kirchoff migration of the CD-ROM data set has shown little improvement in image quality [Morozov and Dueker, 2002; Morozov and Dueker, 2003].

To find our model vector, this matrix formulation is iteratively solved via re-weighted back-projection (Eqn. 3 and 4). To down weight the effects of noisy data, the data misfit is calculated and used to re-weight the system of equations using the data covariance matrix $\mathbf{C_d}$. In practice, only two iterations are used, which has the effect of down weighting about 30% of the dataset. The net effect is that the model amplitudes are increased and the variance reduction increases from 30% to 60%; however, no new structure is created in the process. The equation solved is:

$$\left[\mathbf{C_d}^{-1/2} \mathbf{A S} \right] \left(\mathbf{S}^{-1} \mathbf{m} \right) = \mathbf{C_d}^{-1/2} \mathbf{d} \quad (3a)$$

where **S** is a nearest neighbor smoothing matrix. This can be rewritten as

$$\mathbf{A'} = \mathbf{C_d}^{-1/2} \mathbf{A S}, \quad \mathbf{d'} = \mathbf{C_d}^{-1/2} \mathbf{d}, \quad \mathbf{m'} = \mathbf{S}^{-1} \mathbf{m} \quad (3b)$$

hence:

$$\mathbf{A'\ m'} = \mathbf{d'}. \quad (3c)$$

Direct inversion of the **A**' matrix has been done with a LSQR matrix solver, however the solution requires strong regularization and shows no improvement over simple back-projection [*Shearer et al.*, 1999]. Therefore, our final solution is constructed via simple back projection:

$$\mathbf{m'} = \mathbf{A'}^{t}\,\mathbf{d'}. \qquad (4a)$$

The final model solution **m** is obtained by smoothing the "roughened model" vector **m**' (Eqn. 3b):

$$\mathbf{m} = \mathbf{S}\,\mathbf{m'}. \qquad (4b)$$

To summarize, each model parameter estimate is the mean of the data points "sampling" a given scattering point. The data covariance matrix $\mathbf{C_d}$ is recalculated based upon the residuals of the data to converge towards a more robust solution. A smoothing matrix **S** imposes a horizontal correlation between the three nearest neighbors to either side of each scattering point. This imposes a lateral correlation length of 14 km upon the image. Structures imaged that have length scales less than this correlation length should not be interpreted as real structure.

2.5 Bootstrapping and Error Estimation

An estimate of the model errors can be found by calculating the variance of data at each model point. However, the variance is only a reasonable proxy for error if the underlying probability distributions are Gaussian-like. Therefore, to assess the underlying distributions of the model parameters, bootstrapping with replacement [*Efron and Tibshitani*, 1986] is used. This is done by constructing 100 realizations of the model where each model realization is constructed from a randomly chosen set of waveforms. Then, histograms of each model parameter are constructed to visually assess the Gaussian-like nature of the distributions. This procedure shows that the model distributions are generally bell-shaped in form and not multi-modal. This suggests that the standard errors are a reasonable estimate of the model errors.

2.6 Phasing Analysis and Reverberation Suppression

A primary source of image degradation is the contamination of the image by Pp_dS and Ps_dS crustal reverberations (Fig. 1); thus, a goal of receiver function imaging should be the identification and suppression of these reverberations. The strongest reverberation is the Pp_dS arrival, whereas the Ps_dS reverberation is the superposition of two arrivals (Fig. 1) that can be "split" by lateral velocity heterogeneity, interface dip, or anisotropy making this phase less visible in our images. Reverberation contamination in the images depends on several factors: 1) the dominant period of the data; 2) the depth of the interface; 3) interface dip; 4) lateral crustal velocity variations (both isotropic and anisotropic); 5) the ray parameter distribution of the data.

To suppress reverberations, the mode of the arrival (i.e., P_dS, Pp_dS or Ps_dS) is determined via phasing analysis. The CCP image can then be muted to suppress arrivals that do not display the moveout associated with a direct P_dS arrival. Move-out is the timing difference between a converted phase arrival and its equivalent vertically incident arrival (i.e., p=0). The move-out for a P_dS arrival is:

$$\delta T_{P_dS}(p,z) = T_{P_dS}(p,z) - T_{P_dS}(0,z) \qquad (5)$$

where z is depth of discontinuity, p is ray parameter, $T_{p_dS}(0,z)$ (Eqn. 1a) is the zero incident angle arrival time, and $T_{p_dS}(p,z)$ is the P_dS arrival time. To form a phasing diagram, the moveout for a range of phasing depths is calculated

$$T_{phase}(p,z,z') = \delta T(p,z')_{phase} + T_{phase}(0,z) \qquad (6)$$

where phase is P_dS, Pp_dS or Ps_dS, p is the ray parameter for a given ray, z' is the trial phasing depth and z is the depth. A mode is said to phase when the maximum amplitude in the phasing plot resides close to the z=z' line.

To apply this phasing algorithm to our 2-D spatial image, the raw image is divided into overlapping spatial panels (Plate 2a). These panels are 16 km wide that corresponds to the lateral correlation scale length imposed by our S matrix (Eqn. 3a). A 50% spatial overlap between panels is used to smooth the results. In each data panel, a phasing plot is constructed (Plate 2b). To select which arrivals to further analyze, the standard deviation of each phasing panel is calculated. Any arrivals with an amplitude greater than two standard deviations above the average are identified as candidate arrivals.

To determine the phasing errors of these arrivals, each candidate arrival is bootstrapped 100 times (Plate 2c) and the coordinates (z and z') of the peak value are recorded. Then, each arrival that is close to the line of perfect phasing (z=z') are selected (Plate 2b). A two dimensional Guassian is fitted to the bootstrapped distribution of peak phasing values (Plate 2c). To construct the 1-D muting function, the ensemble of 2-D Guassian distributions are evaluated along the line of optimal phasing (Plate 2d). Finally, the 1-D muting functions for each panel are interpolated to generate a 2-D weighting function that is then applied to the raw image to create the phase muted image (Plate 2e).

The phasing analysis ability to resolve the moveout of our data depends on the dominant period of the data (i.e. the move-out needs to be > ¼ the dominant period of the waveforms). Equation 1 predicts that an interface at 40 km has up to 2.0 s of differential move-out between P_ds and Pp_ds arrivals (Fig. 3). The 2.0 s of move-out between P_ds and Pp_ds is resolvable with respect to the 1-2 s dominant period of the data. The caveats are that the interface is nearly flat (i.e., <10 % dip) and that a wide distribution of ray parameters (p=0.04 to 0.1 s/km) is available.

To test the robustness of the phasing analysis, a suite of synthetic receiver functions have been made. Plate 2 shows the results of one such test with discontinuities placed at 25, 40 and 120 km. The signals for the receiver functions are constructed using equation 1 and contain the direct and two primary reverberations. To simulate realistic velocity heterogeneity, a random time picked from a Gaussian distribution with a half width of 0.5 s was added to the timing of each arrival. The deconvolution and signal generated noise are simulated by randomly selecting rescaled receiver functions and adding them to each synthetic receiver function. This noise simulation consists of taking 80 s segments with a random start time between 2-22 s of the P-arrival and scaling the RMS value to 1/3 the amplitude of the synthetic arrivals to approximate the signal to noise ratio of the data [Morozov and Dueker, 2003]. The same filter used for real data is applied to the synthetics. This synthetic receiver function dataset was constructed using the CD-ROM south ray paths (Fig. 2). The results of this test indicate that this technique can distinguish layers that are separated by >10 km with 1-2 s dominant period data.

2.7 Identification of lithosphere

A fundamental question is whether our mantle layering resides in the lithosphere or asthenosphere. We propose that the creation of strong, horizontal layering in the asthenosphere is difficult and therefore any observed layering resides in the lithosphere. The only well accepted solid-state phase transition between the Moho and 200 km depth range is the spinel to garnet transition [*Anderson*, 1989]. However, this transition is both small in amplitude and has a broad phase loop incapable of producing the amplitudes observed in our images. Chemical layering in the asthenosphere can be ruled out as most researchers believe the asthenosphere is convectively mixed [*Helffrich and Wood*, 2001] and chemical layering in the asthenosphere could only be maintained if the asthenosphere is not convecting. Another mechanism capable of producing velocity layering in the asthenosphere would be the proposed change in the dominant creep mechanism from dislocation to diffusion creep [*Karato and Wu*, 1993]. However, this creep transition is thought to only occur in cool, high stress regions of the mantle, not the warmer, lower stress asthenosphere. Thus, lithospheric layering seems more plausible especially given the observation of strong chemical layering in xenolith columns [*Griffin et al.*, 1999], flat slabs juxtaposing oceanic crust against peridotite mantle [*Bostock*, 1998] and mantle shear zones associated with the collisional tectonics [*Levin and Park*, 2000].

3. RESULTS

For comparison the raw and reverberation suppressed images of lithosphere layering are shown in Plate 3 and 4, albeit interpretation will primarily be focused on the reverberation suppressed image. Note the Moho arrival phases well as a P_ds arrival and is not suppressed by the muting function (Plate 4). The Moho Pp_ds reverberation underneath the south line (reverberation falsely mapped to ~175 km depth) is muted because it did not phase as a P_ds arrival. For the

north line, the reverberations from the Moho are not clearly visible (Plate 4), most likely due to the large amount of Moho topography and a smaller data set.

3.1 North Line

Differences between the Archean and Proterozoic lithospheres are observed in crustal thickness and sub-crustal reflectivity. Underneath the Cheyenne belt the crust is ~40 km thick, at the Proterozoic south end of the line the crust is ~50 km thick and at the Archean north end of the line the crust is ~40 km thick. Evidence for suturing tectonics is suggested by the image of an imbricated Moho just north of the Cheyenne suture, where the Proterozoic crust appears thrust under the Archean crust. The spatial density and lateral continuity of the sub-crustal structure varies north and south of the Cheyenne belt. The mantle layering in the Proterozoic sub-crustal region truncates approximately below the Cheyenne Belt. This subtle change in structure across the Cheyenne suture supports the notion that the lithosphere on either side is different. There is a lack of sub-crustal structure underneath the rifted 2.1 Ga rifted margin Archean crust. As discussed previously, the sub-crustal layering is interpreted as lithospheric in origin, which implies a lithosphere that is at least 150 km thick. Interestingly, the region in-between the Proterozoic lithosphere and the Archean rifted margin is devoid of sub-crustal reflectivity. At the northern end of this line, Archean sub-crustal layering is observed. The depth of this layering deepens to the north and is interpreted to manifest the southern margin of the 2.1 Ga rifted lithosphere.

Mid-crustal features imaged under the Cheyenne belt, correspond well with CD-ROM seismic reflection profiles [*Morozova et al*, this volume; *Tyson et al*, 2002]. Downward projection of the Cheyenne suture reveals mid-crustal features that correspond to the reflectivity "wedge" imaged in the reflection profile.

3.2 South Line

The southern line crosses four physiographic provinces: Mazatzal province to the south of the Jemez volcanic lineament; the 100 km wide Jemez volcanic lineament; southern Yavapai province between the Jemez and Rio Grande rift; the Rio Grande rift. The Moho is relatively flat across the transect at a depth of ~ 40 km, with small changes in the thickness of the crust occurring at the northern edge of the Jemez volcanic lineament and southern end of the Rio Grande rift. Underneath the Jemez volcanic lineament structural variations are observed in the crust. To the south and to the north of the Jemez volcanic lineament a strong mid-crustal discontinuity is observed at ~15 km depth. Below the Jemez volcanic lineament a weaker discontinuity is observed at ~20 km depth. A series of S-dipping mid-crustal reflections observed in the CD-ROM seismic reflection experiment suggests that a paleo-subduction exist to the north of the Jemez volcanic lineament [*Maganai and Levander*, this volume]. The south dipping paleo-subduction is broadly consistent with a step in the Moho and truncation of the crust and mantle layering.

The subcrustal lithosphere in this region is defined by two laterally coherent layers at ~60 and 85 km. The most profound sub-crustal layering is present beneath the Jemez volcanic lineament where coherent layering extends from the Moho to 100 km. The sub-crustal discontinuities show structural changes to the north and south of the Jemez volcanic lineament Below 100 km, there is structure that is comparable to that observed in the north, therefore the lithosphere is interpreted to be at least 100 km thick and perhaps thicker.

3.3 Integrated tomography – receiver functions

Shear-wave splitting, tomographic velocity images and our mantle layering results suggest a complex history of continental-island arc collisions and lithosphere development and modification. To elucidate the origin of the observed mantle layering, the correlation between the tomographic velocity image [*Yuan and Dueker*, this volume] and mantle layering are assessed (Plate 5).

When comparing the receiver functions with the regional tomography, an understanding of what information is contained in these techniques and how this information is complementary is required. Receiver functions image sharp vertical gradient of velocity and tomography images volume velocity variations. These two methods provide complementary information.

Comparison of the two images (Plate 5) reveals several correlations. In the northern line, the fast "slab" anomaly is in a region largely devoid of sub-crustal layering. The upper surface of this velocity anomaly truncates layering in the

Archean lithosphere to the north. On the southern line, a slow velocity anomaly is observed between 40-100 km depth beneath the Jemez lineament. This is where the strongest sub-Moho lithospheric layering is observed.

4. DISCUSION

Beneath the North line, the truncation of Archean mantle layering against the top of the high-velocity "slab" is consistent with the slab's tectonic emplacement after the creation of the 2.1 Ga rifted margin. The slab's upper surface, beneath the imbricated Moho, is consistent with the slab emplacement perhaps "driving" the crustal imbrication. We propose that the imbricated Moho (Plate 5), and north dipping high-velocity anomaly [*Yuan and Dueker*, this volume], are the remnants of a short-lived subduction zone that flipped polarity during the Proterozoic accretion events [Tyson et al, 2002]. The evolutionary scenario is: 1) layered Archean mantle exists pre-rifting; 2) rifting reshaped the edge of continental lithosphere into a sloping boundary [*Buck*, 1991]; 3) the slab fragment is emplaced against this lithospheric boundary via a post-collision polarity flip [Tyson et al, 2003]. Subduction zone polarization reversal are observed today in Taiwan [*Chemenda et al.*, 2001; *Teng et al.*, 2000] and at the Banda arc [*Snyder and et al.*, 1996].

The New Mexico mantle lithosphere is best defined by its layered structure and high heat flow. Under the Jemez volcanic lineament, a low velocity body is imaged down to 100 km depth (Plate 5)[Yuan and Dueker, this volume]. Models to explain this low velocity body are: 1) active upwelling from below (i.e. a plume) eroding the lithosphere; 2) passive asthenospheric upwelling from rifting lithosphere; 3) low-solidus heterogeneities in the lithosphere associated with hydrated regions and/or basaltic dykes [*Carlson and Irving*, 1994]. Major passive upwelling is unlikely because the Jemez lineament has not undergone any major extension. The Jemez low velocity anomaly is 50-100 km off axis from the Rio Grande Rift that has a total net extension of <20 km [*Chapin and Cather*, 1994] and is currently extending at <1 mm/yr [*Thatcher et al.*, 1999]. This small amount of crustal thinning cannot fully explain the high heat flow, indicating that another mechanism is needed to generate this heat [*Keller et al.*, 1990].

Our preferred model is that the Jemez low velocity anomaly and mantle layering define the minimum lithospheric thickness. If the mantle beneath the Jemez volcanic lineament is low-solidus mantle, then this mantle could reduced the velocities due to small melt fractions. Given that the Jemez lineament is a suture between the Yavapai and Mazatzal provinces, this region may have been hydrated by Proterozoic subduction [*Selverstone et al.*, 1999]. In this case, the Jemez volcanism would be an indicator of the "fertility" of the Mazatzal – Yavapai suture zone. The high heat flow in this region suggests that the base of the lithosphere is being heated.

5. CONCLUSION

Our results indicate structural differences preserved in the mantle lithosphere between the Wyoming Archean province and Proterozoic island arc terranes. This result supports the proposal that the lithosphere underneath the north line is thick, old and stable. On the other hand, continental lithosphere under the south line has been modified in recent times by rifting and magmatic events and is 100 km thick. The Jemez volcanic lineament may mark a hydrated Proterozoic-Proterozoic suture zone. The Wyoming Archean lithosphere is cold and at least 150 km thick (strong and stable) and is relatively unaffected by the warm asthenosphere to the south.

Acknowledgements. This work was made possible by the IRIS/PASSCAL instrumentation pool and by a grant from the National Science Foundation Continental Dynamics Program (EAR-9614862).

FIGURE CAPTIONS

Figure 1. Ray diagram showing seismic response from one discontinuity. (A) Ray paths for the three primary converted phases shown: the direct arrival (P_dS) and two free-surface reverberations (Pp_dS and Ps_dS). (B) The relative arrival times, amplitudes and polarities predicted for these phases.

Figure 2. CD-ROM ray-set characteristics. (A) The distribution of earthquake back-azimuths for all data. (B) The distribution of direct P ray parameters, a wide distribution is needed to properly phase arrivals as outlined in section 3.6. (C) Converted S-wave ray coverage.

Figure 3. Move-out curves for discontinuity at 40 km depth. The curves are for P_ds and Pp_ds move-out. The three curves for each phase represent the change in move-out with a +/- 5% anti-correlated change in Vp and Vp/Vs with respect to our 1-D velocity model. Note the maximum differential move-out between P_ds and Pp_ds is 2.5 s, which is distinguishable in our phasing analysis using data with a 1-2 s dominant period.

Plate 1. Continental Dynamics – Rocky Mountains (CD-ROM) PASSCAL passive broad-band deployment. Base map of the Rocky Mountain region encompassing the states of Wyoming (WY), Colorado (CO) and New Mexico (NM). Major geological boundaries are shown as black lines [*CD-ROM working group*, 2002]. Seismic stations are denoted by triangles. Seismic transect is indicated A-A'. Volcanic fields of interested are marked by 'X' and their geographic labels are denoted as: LH – Lucite Hills, IM – Iron Mountain, SL – State Line, SBL – Steamboat lamproites, MPL – Middle Park lamproite, OVF – Ocate volcanic field, JVF – Jemez volcanic field

Plate 2. Phasing analysis of synthetic receiver function stacks using CD-ROM south line ray set. Velocity discontinuities have been placed at 25, 40 and 120 km. P_ds, Pp_ds and Ps_ds phases are included in the synthetic receiver functions. Noise was added using randomly selected waveform segments. (A) Common conversion point image. Notice that the deeper the discontinuity, the more incoherent its reverberations becomes because the reverberations are being mis-stacked using the P_ds move-out curves. (B) Phasing diagram for P_ds (right half) and Pp_ds arrivals (left half). The Pp_ds target depth axis has been mapped to P_ds depth to facilitate comparison between direct and reverberated converted arrivals. The peak values at which arrivals are phased are marked by a '+' and the associated standard deviations are indicated by the ovals. (C) Bootstrapped mean phasing location. Circles represent the phasing location for each bootstrapped iteration. The oval represents the 2-D Gaussian distribution fitted to the bootstrapped phasing peaks. (D) Muting function derived from evaluating phasing probabilities along the line of optimal phasing (z=z') in (b). (E) Muted image derived by multiplying each data panel by its corresponding mute function**.**

Plate 3. Crust and mantle layering images. (A) North transect. (B) South transect. Amplitudes are normalized with respect to the mean Moho amplitude. The variance reduction of the model was 69%. No vertical exaggeration is applied. Geological surface boundaries are labeled: OVF- Ocate volcanic field, RIO- eastern edge of Rio Grande rift; FW SZ- Farwell mountain shear zone.

Plate 4. Muted crust and mantle layering images. (A) North transect. (B) South transect. Phasing panels are 16 km wide with 50% sharing between panels. The same amplitude scale is used as Plate 3. No vertical exaggeration is applied. Geological surface boundaries are labeled as Plate 3.

Plate 5. Lithospheric layering and P-wave tomographic image. (A) The non-muted model (Plate 3) (B) the muted image (Plate 4). Blue discontinuity shading denotes a positive shear wave contrasts and red denotes a negative shear wave contrast. The tomographic velocity anomalies are denoted by the transparent overlays. The red overlay denotes the region with >2% low velocity anomaly and the blue overlay is the >2% high velocity anomaly. [*Yuan and Dueker*, this volume]. Transect is shown in Figure 1 as A-A''. Geological surface boundaries are labeled as following: CB- Cheyenne belt, FW-SZ - Farwell Mountain shear zone, RIO- eastern edge of Rio Grande rift, OVF- Ocate volcanic field. No vertical exaggeration is applied.

Southern Rocky Mountain Lithospheric Structure

Brian Zurek and Ken Dueker

REFERENCES

Anderson, D. L., *Theory of the Earth*, 367 pp., Blackwell Scientific Publications, Boston, 1989.

Balling, N., Deep seismic reflection evidence for ancient subduction and collision zones within the continental lithosphere of northwestern Europe, *Tectonophysics*, *329* (1-4), Pages 269-300, 2000.

Bank, C. G., M. G. Bostock, R. M. Ellis, and J. F. Cassidy, A reconnaissance teleseismic study of the upper mantle and transition zone beneath the Archean Slave Craton in NW Canada, *Tectonophysics*, *319* (3), Pages 151-166, 2000.

Bird, P., Continental delamination and the Colorado Plateau, *Journal of Geophysical Research*, *84* (B13), 7561-7571, 1979.

Bird, P., Formation of the Rocky Mountains, western United States: a continuum computer model, *Science*, *239* (4847), 1501-1507, 1988.

Bostock, M. E., Anisotropic upper-mantle stratigraphy and architecture of the Slave Craton, *Nature (London)*, *390* (6658), Pages 392-395, 1997.

Bostock, M. G., Ps conversions from the upper mantle transition zone beneath the Canadian landmass, *Journal of Geophysical Research, B, Solid Earth and Planets*, *101* (4), Pages 8383-8402, 1996.

Bostock, M. G., Mantle stratigraphy and evolution of the Slave Province, *Journal of Geophysical Research B: Solid Earth*, *103* (B9), 21,183-21,200, 1998.

Buck, W. R., Modes of continental lithospheric extension, *Journal of Geophysical Research*, *96* (B12), 20,161-20,178, 1991.

Carlson, R. W., and A. J. Irving, Depletion and enrichment history of subcontinental lithospheric mantle: an Os, Sr, Nd and Pb isotopic study of ultramafic xenoliths from the northwestern Wyoming Craton, *Earth & Planetary Science Letters*, *126* (4), 457-472, 1994.

CD-ROM working group, Structure and Evolution of the Lithosphere Beneath the Rocky Mountains: initial results from the CD-ROM experiment, *GSA Today*, *12* (3), 4-10, 2002.

Chapin, C. E., and S. M. Cather, Tectonic setting of the axial basins of the northern and central Rio Grande rift, in *Basins of the Rio Grande Rift: Structure, Stratigraphy and Tectonic Setting*, edited by G.R. Keller, and S.M. Cather, pp. 5-26, Geological Society of America, Boulder, 1994.

Chemenda, A. I., E. A. Konstantinvskaya, G. M. Ivanov, R. K. Yang, and J. F. Stephan, New results from physical modelling or arc-continent collision in Taiwan: Evolutionary model, *Tectonophysics*, *333* (1-2), 159-178, 2001.

Clauser, R. H., and C. A. Langston, Modeling P-Rg coversions from isolated topographic features near the NORESS array, *Bulletion Seismological Society America*, *85*, 859-873, 1995.

Clayton, R. W., and R. A. Wiggins, Source shape estimation and deconvolution of teleseismic body waves, *Geophys. J. R. Astron. Soc.*, *47*, 151-177, 1976.

Deep Probe working group, Probing the Archean and Proterozoic Lithopshere of Westren North America, *GSA Today*, *8* (7), 1-5, 1998.

Dueker, K., H. Yuan, and B. Zurek, Thick-structured Proterozoic lithosphere of the Rocky Mountain region, *GSA Today*, *11* (12), Pages 4-9, 2001.

Dueker, K. G., and A. F. Sheehan, Mantle discontinuity structure from midpoint stacks of converted P and S waves across the Yellowstone hotspot track, *Journal of Geophysical Research*, *102* (B4), 8313-8327, 1997.

Efron, B., and R. Tibshitani, Bootstrap methods for standard errors, confidence intervals, and other measures of statistical accuracy, *Stat. Sci*, *1*, 54-77, 1986.

Frost, B. R., D. Frost Carol, H. Lindsley Donald, S. Scoates James, and N. Mitchell Jeremy, The Laramie anorthosite complex and Sherman Batholith; geology, evolution, and theories of origin, *Memoir Geological Survey of Wyoming*, *5*, 118-161, 1993.

Goes, S., and S. van der Lee, Thermal structure of the North American uppermost mantle inferred from seismic tomography, *Journal of Geophysical Research B: Solid Earth*, *107* (B3), ETG 2, 2002.

Grand, S. P., and D. V. Helmberger, Upper mantle shear structure of North America, *Geophysical Journal-Royal Astronomical, Society*, 399-438, 1984.

Griffin, W. L., S. Y. O'Reilly, R. Davies, K. Kivi, E. van Achterbergh, L. M. Natapov, B. J. Doyle, C. G. Ryan, and N. J. Pearson, Layered mantle lithosphere in the Lac de Gras area, Slave craton: Composition, structure and origin, *Journal of Petrology*, *40* (5), 705-727, 1999.

Gurrola, H., J. B. Minster, and T. Owens, The use of velocity spectrum for stacking receiver, *Geophysical Journal International*, *117* (2), 1994.

Helffrich, G. R., and B. J. Wood, The Earth's mantle, *Nature*, *412* (6846), 501-507, 2001.

Heller, P., K. Dueker, and M. McMillan, Post-Paleozoic alluvial gravel transport as evidence of continental tilting in th U.S. Cordillera, *GSAB*, *115* (9), 1122-1132, 2003.

Jones, C. H., J. R. Unruh, and L. J. Sonder, The role of gravitational potential energy in active deformation in the southwestern United States, *Nature*, *381* (6577), 37-41, 1996.

Karato, S., and P. Wu, Rheology of the upper mantle: a synthesis, *Science*, *260* (5109), 771-778, 1993.

Karlstrom, K. E., and S. A. Bowring, Early Proterozoic assembly of tectonostratigraphic terranes in southwestern North America, *Journal of Geology*, *96* (5), 561-576, 1988.

Karlstrom, K. E., and R. S. Houston, The Cheyenne belt: analysis of a Proterozoic suture in southern Wyoming, *Precambrian Research*, *25* (4), 415-446, 1984.

Keller, G. R., P. Morgan, and W. R. Seager, Crustal structure, gravity anomalies and heat flow in the southern Rio Grande rift and their relationship to extensional tectonics, *Tectonophysics*, *174* (1-2), 21-37, 1990.

Kennett, B. L. N., and E. R. Engdahl, Traveltimes for global earthquake location and phase identification, *Geophysical Journal International*, *105* (2), 429-465, 1991.

Langston, C. A., Corvallis, Oregon, crustal and upper mantle receiver structure from telesismic P and S waves, *Bulletion Seismological Society America*, *67*, 713-724, 1977.

Levander, A., and N. R. Hill, P-SV resonances in irregular low-velocity surface layers, *Bulletion Seismological Society America*, *75*, 847-864, 1985.

Levin, V., and J. Park, Shear zones in the Proterozoic lithosphere of the Arabian Shield and the nature of the Hales discontinuity, *Tectonophysics*, *323* (3-4), Pages 131-148, 2000.

McCallum, M. E., D. H. Eggler, and L. K. Burns, Kimberlitic diatremes in northern Colorado and southern Wyoming, *Physics and Chemistry of the Earth*, *9*, 149-161, 1975.

Morgan, P., and W. D. Gosnold, Heat flow and thermal regimes in the continental United States, in *Geophysical Framework of the Continental United States*, edited by L.C. Pakiser, and W.D. Mooney, pp. 493-522, Geol. Soc. Am., 1989.

O'Reilly, S. Y., W. L. Griffin, Y. H. Poudjom Djomani, and P. Morgan, Are lithospheres forever? Tracking changes in subcontinental lithospheric mantle through time, *GSA Today*, *11* (4), 4-10, 2001.

Rondenay, S., G. Bostock Michael, M. Hearn Thomas, J. White Donald, H. Wu, G. Senechal, S. Ji, and M. Mareschal, Teleseismic studies of the lithosphere below the Abitibi-Grenville Lithoprobe transect, *Canadian Journal of Earth Sciences = Revue Canadienne des Sciences de la Terre*, *37* (2-3), Pages 415-426, 2000.

Selverstone, J., A. Pun, and C. Condie Kent, Xenolithic evidence for Proterozoic crustal evolution beneath the Colorado Plateau, *Geological Society of America Bulletin*, *111* (4), Pages 590-606, 1999.

Shearer, P. M., M. P. Flanagan, and M. A. H. Hedlin, Experiments in migration processing of SS precursor data to image upper mantle discontinuity structure, *Journal of Geophysical Research B: Solid Earth*, *104* (4), 7229-7242, 1999.

Smith, D., Insights into the evolution of the uppermost continental mantle from xenolith localities on and near the Colorado Plateau and regional comparisons, *Journal of Geophysical Research B: Solid Earth*, *105* (7), 16,769-16,781, 2000.

Snyder, D. B., and et al., A dual doubly vergent orogen in the Banda Arc continent-arc collision zone as observed on deep seismic reflection profiles, *Tectonics*, *15* (1), 34-53, 1996.

Teng, L. S., C. T. Lee, Y. B. Tsai, and L. Y. Hsiao, Slab breakoff as a mechanism for flipping of subduction polarity in Taiwan, *Geology*, *28* (2), 155-158, 2000.

Thatcher, W., E. Quilty, G. W. Bawden, G. R. Foulger, B. R. Julian, and J. Svarc, Present-day deformation across the Basin and Range Province, western United States, *Science*, *283* (5408), 1714-1718, 1999.

Thompson, G. A., and M. L. Zoback, Regional geophysics of the Colorado Plateau, *Tectonophysics*, *61* (1-3), 149-181, 1979.

Thompson, R. N., J. G. Mitchell, A. P. Dickin, S. A. Gibson, D. Velde, P. T. Leat, and M. A. Morrison, Oligocene lamproite containing an Al-poor, Ti-rich biotite, Middle Park, northwest Colorado, USA, *Mineralogical Magazine*, *61* (4), 557-572, 1997.

Warner, M., J. Morgan, P. Barton, P. Morgan, C. Price, and K. Jones, Seismic reflections from the mantle represent relict subduction zones within the continental lithosphere, *Geology (Boulder)*, *24* (1), Pages 39-42, 1996.

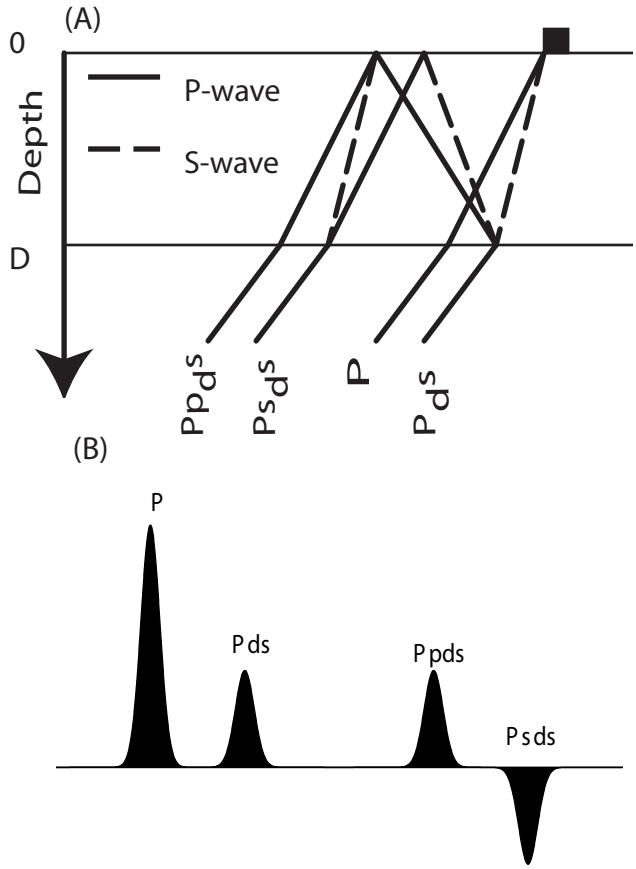

Figure 1

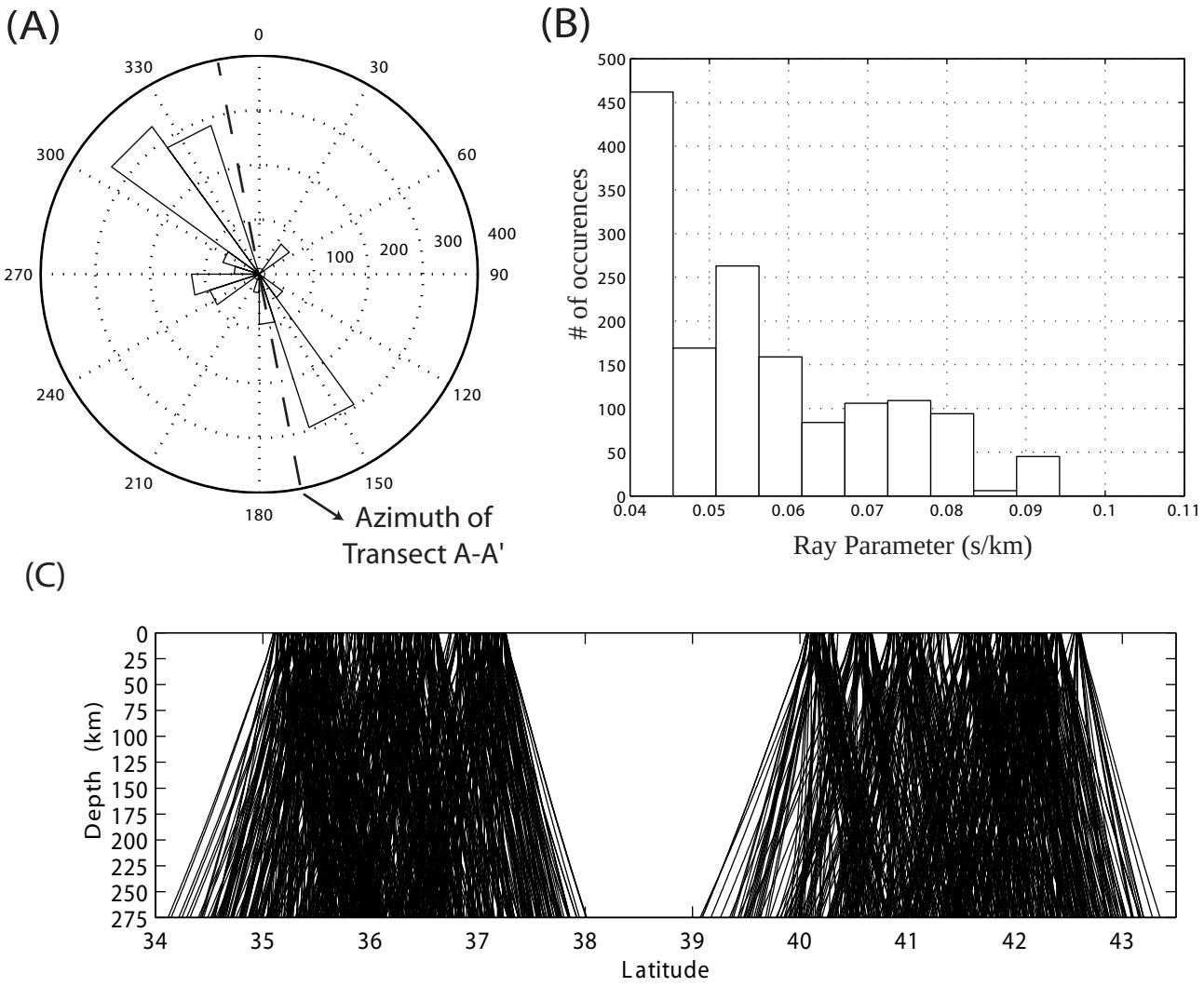
(A)
0
30
60
90
120
150
180
210
240
270
300
330
100
200
300
400
Azimuth of
Transect A-A'
(B)
# of occurences
Ray Parameter (s/km)
(C)
Depth (km)
Latitude

Figure 2

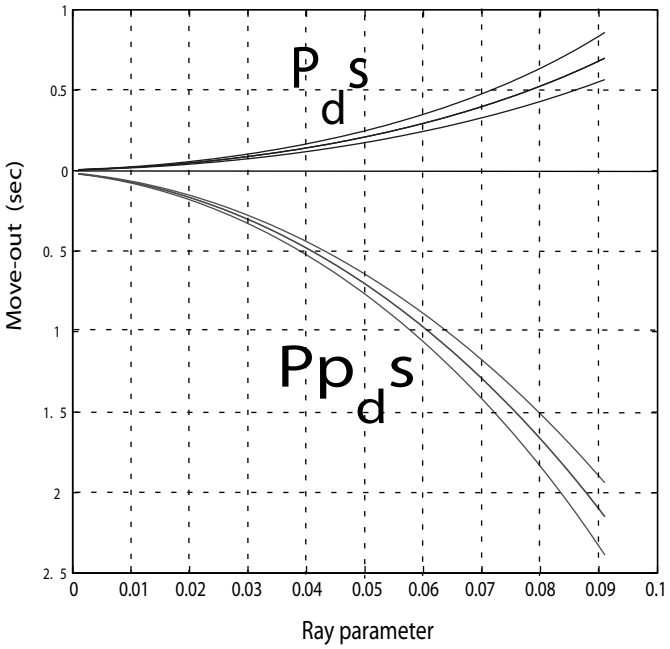
P s
d
Pp s
d
Move-out (sec)
Ray parameter
1
0.5
0
0. 5
1
1. 5
2
2. 5
0
0.01
0.02
0.03
0.04
0.05
0.06
0.07
0.08
0.09
0.1

Figure 3

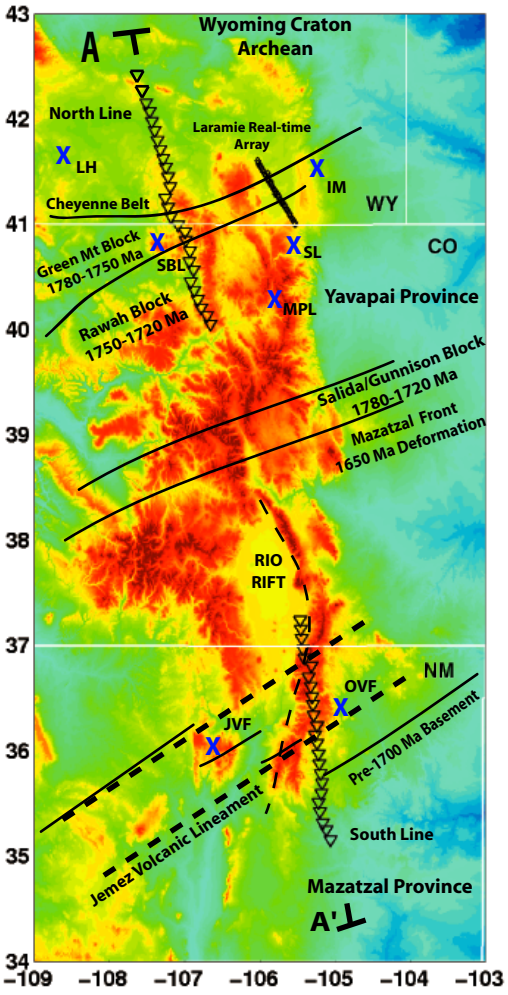
A
T
Wyoming Craton
Archean
North Line
Laramie Real-time
Array
LH
IM
WY
Cheyenne Belt
Green Mt Block
1780-1750 Ma
SBL
SL
CO
Rawah Block
1750-1720 Ma
MPL
Yavapai Province
Salida/Gunnison Block
1780-1720 Ma
Mazatzal Front
1650 Ma Deformation
RIO
RIFT
NM
OVF
JVF
Pre-1700 Ma Basement
South Line
Jemez Volcanic Lineament
Mazatzal Province
A'
T'
43
42
41
40
39
38
37
36
35
34
−109
−108
−107
−106
−105
−104
−103

Plate 1

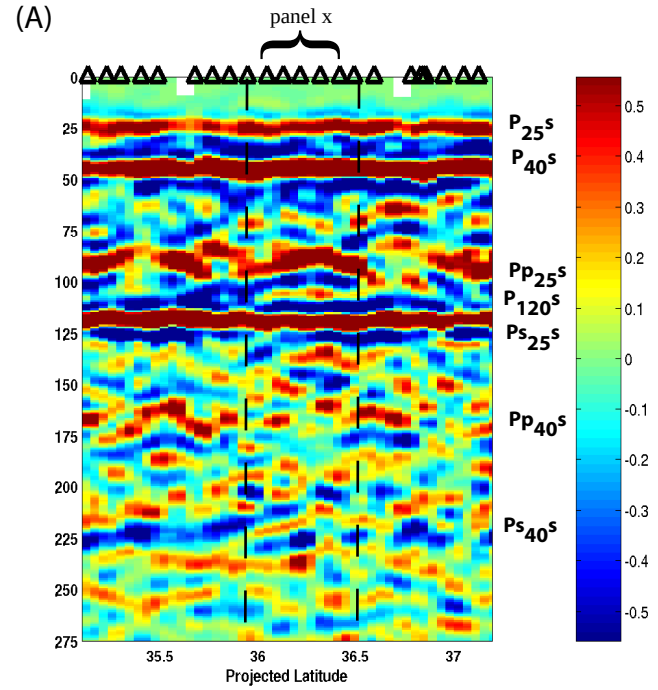
(A)
panel x
P_{25}^s
P_{40}^s
Pp_{25}^s
P_{120}^s
Ps_{25}^s
Pp_{40}^s
Ps_{40}^s
Projected Latitude

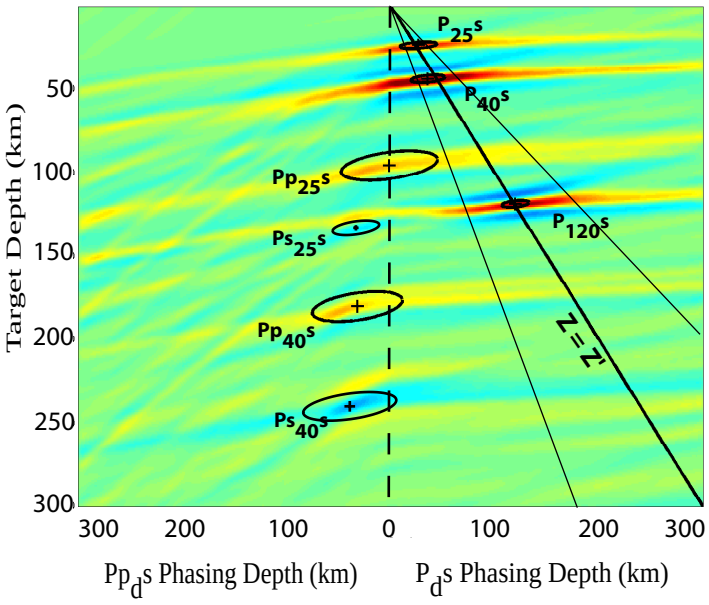
(B)
P_{25}^s
P_{40}^s
Pp_{25}^s
P_{120}^s
Ps_{25}^s
Pp_{40}^s
Ps_{40}^s
Z = Z'
Target Depth (km)
$Pp_d s$ Phasing Depth (km)
$P_d s$ Phasing Depth (km)

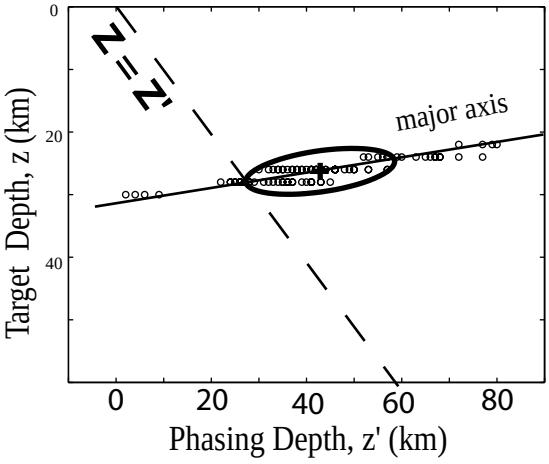
(C)
Z = Z'
major axis
Target Depth, z (km)
Phasing Depth, z' (km)

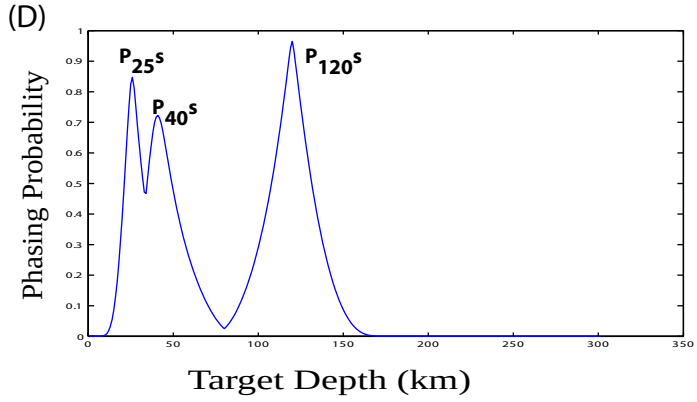
(D)
P_{25}^s
P_{40}^s
P_{120}^s
Phasing Probability
Target Depth (km)

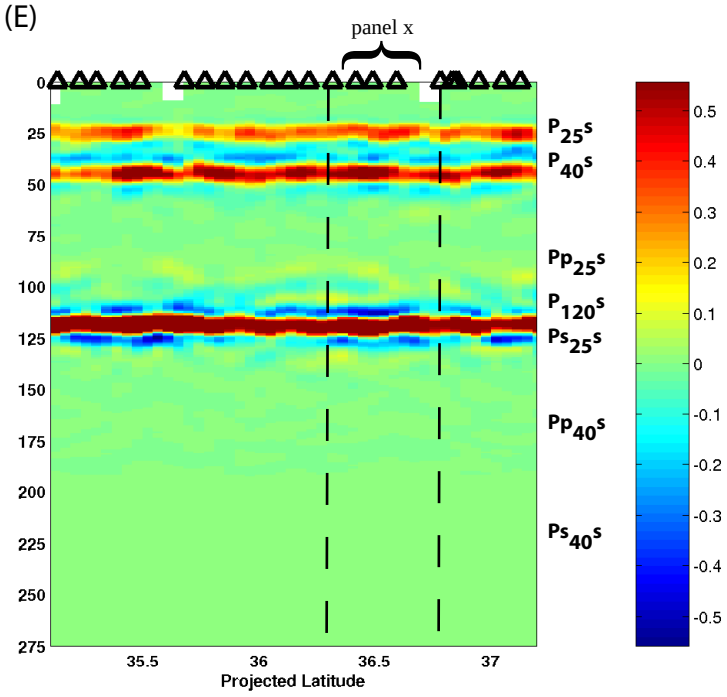
(E)
panel x
P_{25}^s
P_{40}^s
Pp_{25}^s
P_{120}^s
Ps_{25}^s
Pp_{40}^s
Ps_{40}^s
Projected Latitude

Plate 2

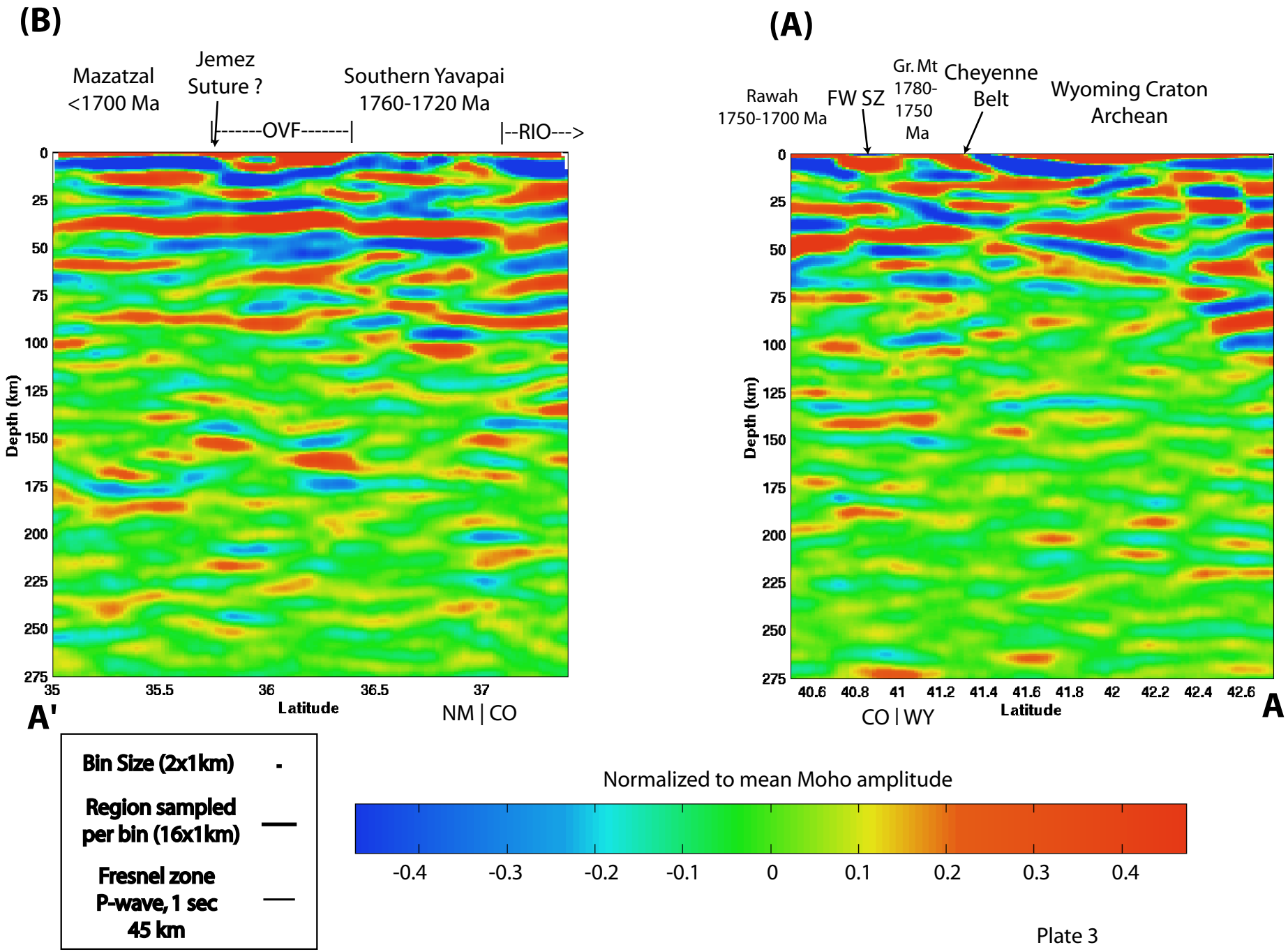
(B)
Mazatzal
<1700 Ma
Jemez
Suture ?
Southern Yavapai
1760-1720 Ma
|-------OVF-------|
|--RIO--->
Depth (km)
0
25
50
75
100
125
150
175
200
225
250
275
35
35.5
36
36.5
37
Latitude
A'
NM | CO
(A)
Rawah
1750-1700 Ma
FW SZ
Gr. Mt
1780-
1750
Ma
Cheyenne
Belt
Wyoming Craton
Archean
Depth (km)
40.6
40.8
41
41.2
41.4
41.6
41.8
42
42.2
42.4
42.6
Latitude
CO | WY
A
Bin Size (2x1km)
Region sampled
per bin (16x1km)
Fresnel zone
P-wave, 1 sec
45 km
Normalized to mean Moho amplitude
-0.4
-0.3
-0.2
-0.1
0
0.1
0.2
0.3
0.4
Plate 3

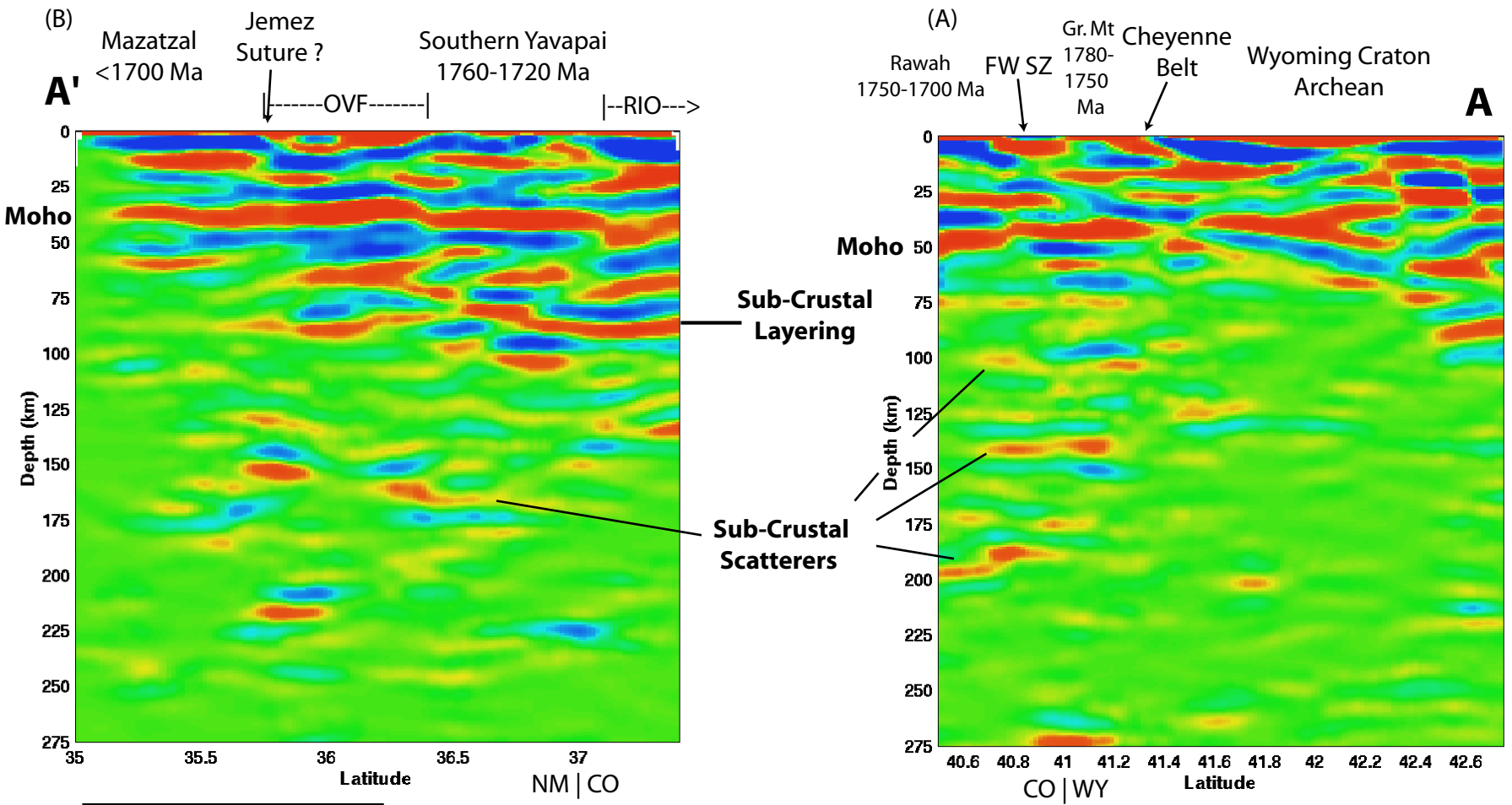
(B)
Mazatzal
<1700 Ma
Jemez
Suture ?
Southern Yavapai
1760-1720 Ma
A'
|-------OVF-------|
|--RIO--->
Moho
Depth (km)
Latitude
NM | CO
Sub-Crustal
Layering
Sub-Crustal
Scatterers
(A)
Rawah
1750-1700 Ma
FW SZ
Gr. Mt
1780-
1750
Ma
Cheyenne
Belt
Wyoming Craton
Archean
A
Moho
Depth (km)
Latitude
CO | WY
Bin Size (2x1km)
Region sampled
per bin (16x1km)
Fresnel zone
P-wave, 1 sec
45 km depth
Normalized to mean Moho amplitude

Plate 4

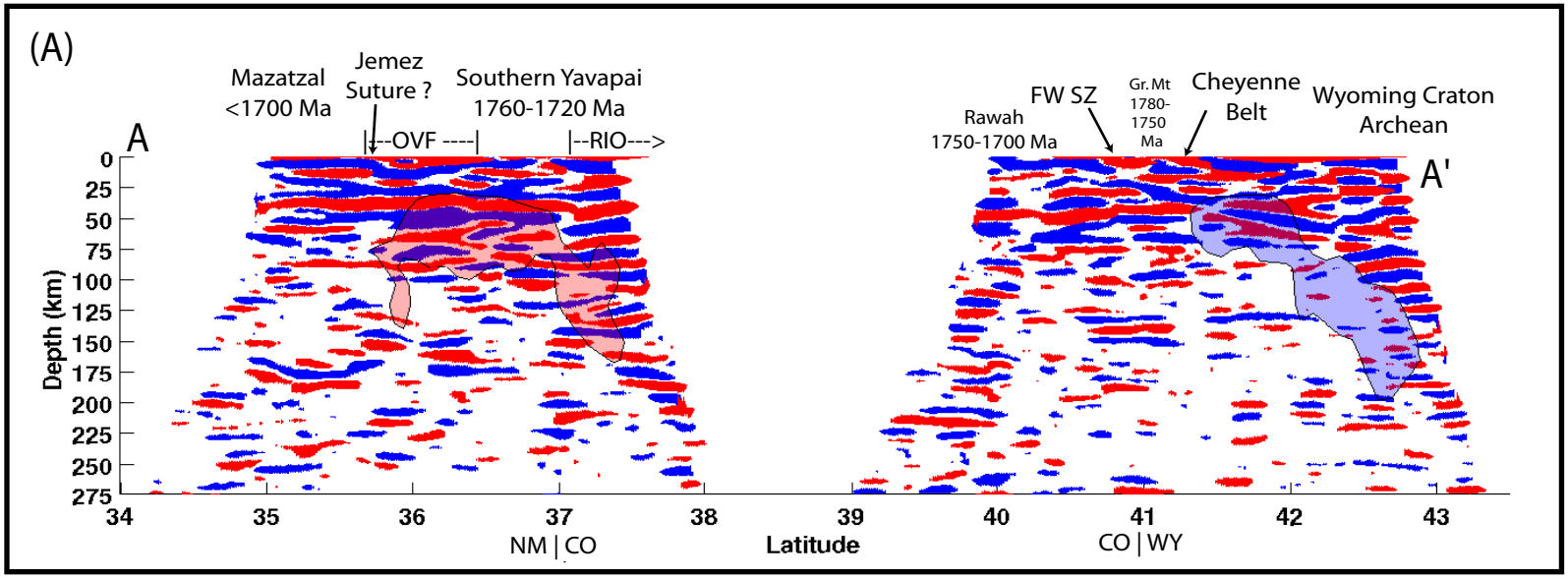
(A)
A
Mazatzal
<1700 Ma
Jemez
Suture ?
Southern Yavapai
1760-1720 Ma
|--OVF ----|
|--RIO--->
Rawah
1750-1700 Ma
FW SZ
Gr. Mt
1780-
1750
Ma
Cheyenne
Belt
Wyoming Craton
Archean
A'
Depth (km)
0
25
50
75
100
125
150
175
200
225
250
275
34
35
36
37
38
39
40
41
42
43
NM | CO
Latitude
CO | WY

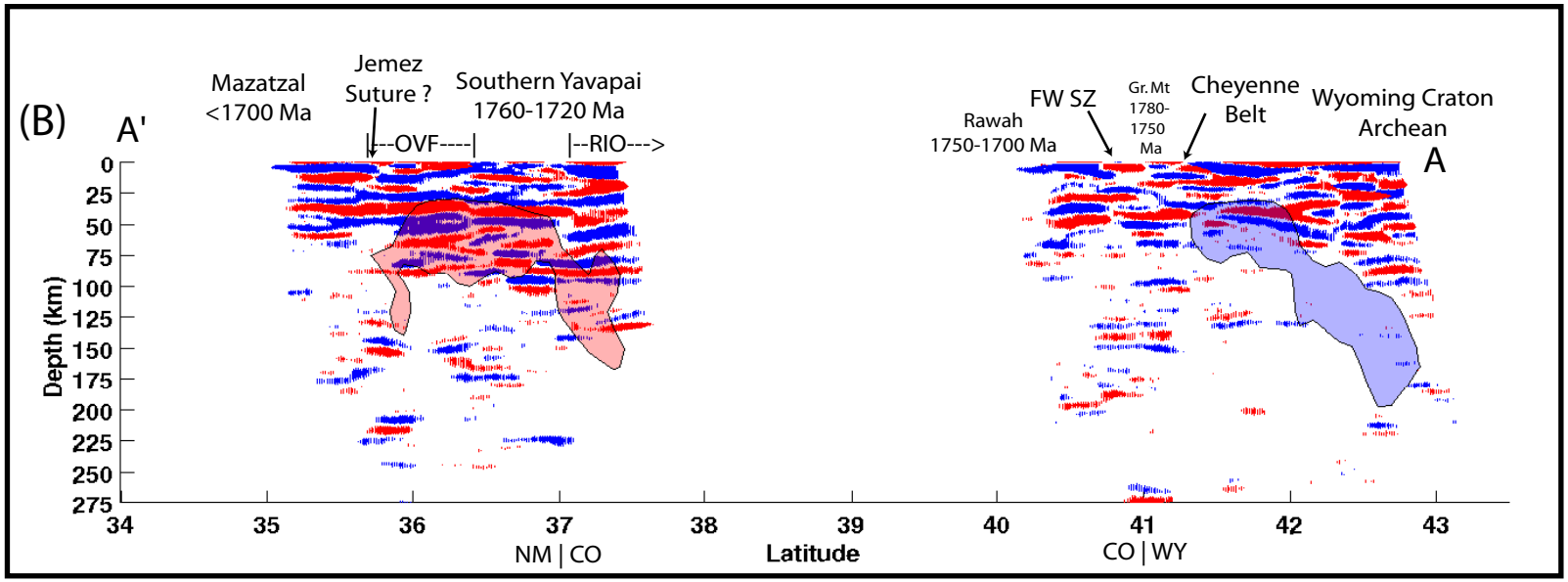
(B)
A'
Mazatzal
<1700 Ma
Jemez
Suture ?
Southern Yavapai
1760-1720 Ma
|--OVF----|
|--RIO--->
Rawah
1750-1700 Ma
FW SZ
Gr. Mt
1780-
1750
Ma
Cheyenne
Belt
Wyoming Craton
Archean
A
Depth (km)
0
25
50
75
100
125
150
175
200
225
250
275
34
35
36
37
38
39
40
41
42
43
NM | CO
Latitude
CO | WY

Plate 5